CrossMark

# *B*-fields and Dust in Interstellar Filaments Using Dust Polarization (BALLAD-POL). I. The Massive Filament G11.11–0.12 Observed by SOFIA/HAWC+

Nguyen Bich Ngoc[1,2] , Pham Ngoc Diep[1,2] , Thiem Hoang[3,4] , Le Ngoc Tram[5] , Nguyen Chau Giang[3,4] , Ngân Lê[6] , Thuong D. Hoang[7] , Nguyen Thi Phuong[1,3] , Nguyen Minh Khang[8] , Dieu D. Nguyen[9] , and Bao Truong[3,4]

[1] Department of Astrophysics, Vietnam National Space Center, Vietnam Academy of Science and Technology, 18 Hoang Quoc Viet, Hanoi, Vietnam
pndiep@vnsc.org.vn
[2] Graduate University of Science and Technology, Vietnam Academy of Science and Technology, 18 Hoang Quoc Viet, Hanoi, Vietnam
[3] Korea Astronomy and Space Science Institute, 776 Daedeokdae-ro, Yuseong-gu, Daejeon 34055, Republic of Korea
[4] University of Science and Technology, Korea, 217 Gajeong-ro, Yuseong-gu, Daejeon 34113, Republic of Korea
[5] Max-Planck-Institut für Radioastronomie, Auf dem Hügel 69, D-53-121, Bonn, Germany
[6] Institute of Astronomy, Faculty of Physics, Astronomy and Informatics, Nicolaus Copernicus University, Grudziądzka 5, 87-100 Toruń, Poland
[7] Center for Data-Driven Discovery, Kavli Institute for the Physics and Mathematics of the Universe (Kavli IPMU, WPI), UTIAS, The University of Tokyo, Kashiwa, Chiba 277-8583, Japan
[8] Institute For Interdisciplinary Research in Science and Education (IFIRSE), ICISE, 07 Science Avenue, Ghenh Rang Ward, 55121 Quy Nhon City, Binh Dinh Province, Vietnam
[9] Université de Lyon1, Ens de Lyon, CNRS, Centre de Recherche Astrophysique de Lyon (CRAL) UMR5574, F-69230 SaintGenis-Laval, France

## Abstract

We report the first measurement of polarized thermal dust emission toward the entire infrared dark cloud G11.11 −0.12 taken by the polarimeter SOFIA/HAWC+ at 214 $\mu$m. The obtained magnetic fields (*B*-fields) from the polarized emission of the early-stage and massive filament tend to be perpendicular to its spine. We produce a map of *B*-field strengths for the center region of the filament. The strengths vary in the range of 100–600 $\mu$G and are strongest along the filament's spine. The central region is sub-Alfvénic and mostly subcritical, meaning that *B*-fields dominate over turbulence and are strong enough to resist gravitational collapse. The alignment and properties of dust grains in the filament are studied using radiative torque (RAT) theory. We find the decrease of polarization degree $P$ with emission intensity $I$, i.e., depolarization effect, of the form $P \propto I^{-\alpha}$ with $\alpha \sim 0.8$–0.9, implying a significant loss of grain alignment in the filament's spine. The depolarization can be explained by the decrease in RAT alignment efficiency toward the denser regions with weaker radiation field, which cannot be explained by *B*-field tangling. We study the effect of the enhanced magnetic relaxation by embedded iron inclusions on RAT alignment and find that the high polarization fraction $P \sim 20\%$–30% in the outer layer of the filament is potential evidence for the magnetically enhanced RAT alignment mechanism. This is the first time this effect is evaluated in a filament. Based on the polarization fraction and RAT alignment theory, we also find evidence for grain growth in the filament.

## 1. Introduction

Observations by Herschel reported the ubiquity of filaments in the interstellar medium (ISM), where prestellar cores and protostars are formed (André et al. 2014). This suggests that filaments can be important stages in the star-forming process. In their earliest phases, several cores can be observed along filaments. Infrared dark clouds (IRDCs) are cradles for the formation of stars, especially high-mass stars and star clusters (e.g., Rathborne et al. 2006). IRDCs are quiescent molecular clouds containing mostly cold and dense molecular gas. The IRDCs would be fragmented to form a number of compact cores and clumps. As they evolve over time, bubbles or H II regions form owing to stellar feedback from massive stars. Then, the filaments will contain bright clusters and appear similar to the filamentary molecular clouds associated with high-mass star-forming regions.

The role of *B*-fields in the formation and evolution of filaments is likely vital because it makes the flows more coherent, allowing filaments to survive longer (see Hennebelle & Inutsuka 2019 for a review). However, the behavior of *B*-fields in filaments is less well understood, in particular, for high-mass stars in their earliest phases. *B*-fields, along with gravity, turbulence, and stellar feedback, are believed to play essential roles in the formation of massive stars (Crutcher 2012).

The measurement of polarized dust emission has become an essential tool for probing *B*-field properties, as the dust grains are preferentially aligned with their major axes perpendicular to the local *B*-field direction (see Lazarian 2007; Andersson et al. 2015 for reviews). From the observed polarized dust emission, the *B*-field morphology can be inferred by rotating the dust polarization angles by 90°. Polarimetric observations at far-infrared (far-IR) and submillimeter wavelengths are widely used to infer the morphology and strengths of *B*-fields (see Pattle & Fissel 2019 for a review). The strengths of the plane-of-sky (POS) component of the *B*-fields can be commonly estimated using the Davis–Chandrasekhar–Fermi method (DCF method; Davis 1951; Chandrasekhar & Fermi 1953).
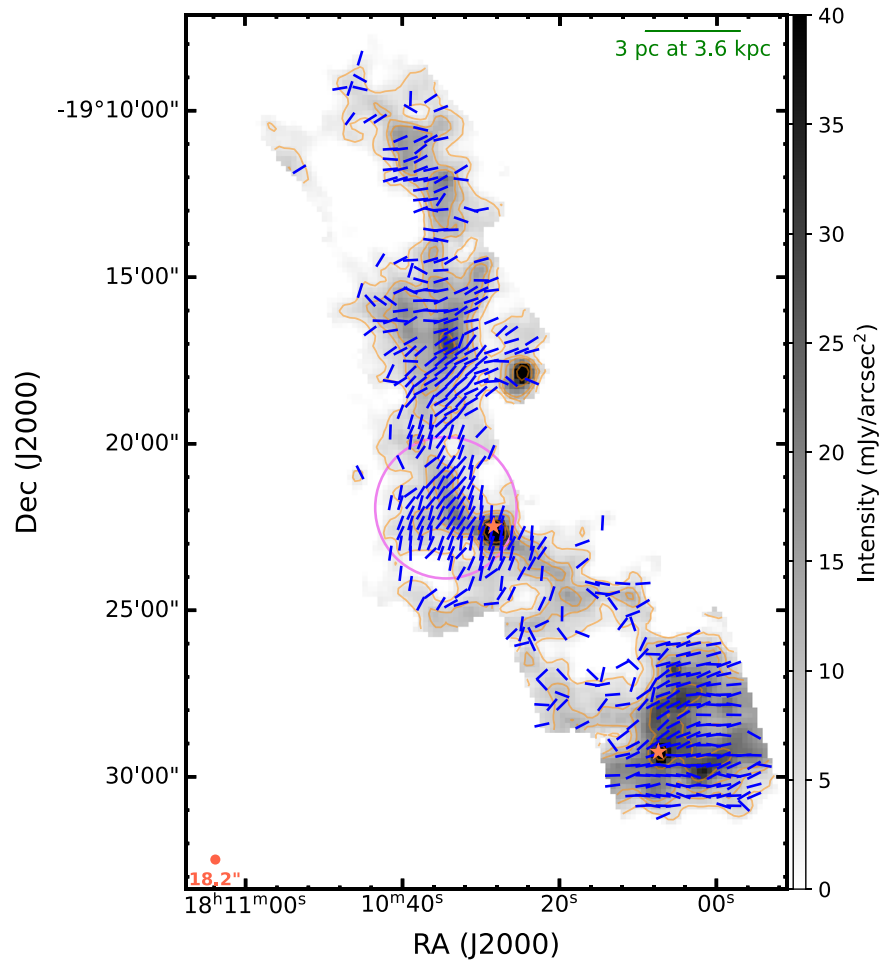
**Figure 1.** Map of $B$-field orientation toward G11 at 214 $\mu$m measured by SOFIA/HAWC+. The blue segments display the $B$-field orientation. The $B$-field segments are plotted such that the spacing between neighboring ones is equal to the beam size. The beam size of SOFIA/HAWC+ at 214 $\mu$m is 18$''$2, which is shown by the red circle in the lower left corner. The $B$-fields are overplotted on a gray map of intensities ($I$). The orange contours are for $I$ = 3.6, 8.4, 12.0, 24.0, 42.0 mJy arcsec$^{-2}$. The red stars mark the locations of two massive protostellar candidates: P1 in the central region and P6 in the southern region (Henning et al. 2010). The violet circle shows the region observed by JCMT/SCUPOL, whose $B$-fields are shown in Figure 2.

Previous studies of $B$-fields toward interstellar filaments using polarized dust emission usually reveal that the $B$-fields are parallel to the filament in diffuse regions and become perpendicular to the filament's spine in dense regions when the hydrogen column density exceeds $N_\mathrm{H} \sim (3\text{–}5) \times 10^{21}$ cm$^{-2}$ (see, e.g., Planck Collaboration et al. 2016; Soler et al. 2017; Soler 2019, for observations; see Soler & Hennebelle 2017, for simulations). To date, there are only a handful of studies about $B$-fields in massive filaments, including G35.39−0.33 (Liu et al. 2018), G34.43 + 0.24 (Soam et al. 2019; Tang et al. 2019), G14.225−0.506 (Añez-López et al. 1919), NGC 6334 (Arzoumanian et al. 2021), and G47.06 + 0.26 (Stephens et al. 2022).

This paper first aims to characterize the properties of $B$-fields in a high-mass star-forming filament G11.11−0.12 (hereafter G11 or colloquially known as the Snake filament). We use data taken by the High-resolution Airborne Wideband Camera Plus (HAWC+; Harper et al. 2018) accommodated on the Stratospheric Observatory for Infrared Astronomy (SOFIA; Temi et al. 2018) at 214 $\mu$m wavelength. We note that $B$-fields in the center region of G11 were studied using the JCMT/SCUPOL polarimetric observations at 850 $\mu$m and 20$''$ (0.35 pc) resolution (Pillai et al. 2015). They found that the $B$-fields toward this region are perpendicular to the filament's spine and

estimated the lower limit of the POS $B$-field strength to be $\sim$200 $\mu$G. This value is converted from the total $B$-field strength using an average field geometry with a conversion factor of 1.3 (Crutcher 2004).

G11 is one of the IRDC filaments in the galactic plane on the near side of the Scutum–Centaurus arm (Wang et al. 2014). It is cold, dense, and in an early phase of evolution (Jackson et al. 2010), in contrast with its late-phase counterparts such as Orion and NGC 6334. G11 is located at a distance of 3.6 kpc from Earth (Pillai et al. 2006), 22 pc long, 1.0 pc wide, and has a mass of $1.5 \times 10^4 M_\odot$ (Zucker et al. 2018). The filament has a linear mass density of $\sim$600 $M_\odot$ pc$^{-1}$, already fragmented, and new stars are expected to be in the process of forming in the filament (Kainulainen et al. 2013). G11 is identified to host seven JCMT/SCUBA clumps (Johnstone et al. 2003) and 18 protostellar cores along its spine (Henning et al. 2010). There are two massive clumps in the filament (P1 and P6 in Figure 1) with a mass of $\sim$1000 $M_\odot$ and sizes less than 1 pc, which are the sites for high-mass star formation (Wang et al. 2014). All these above reasons make G11 an ideal target for studying the initial conditions for the formation of IRDCs with the existence of $B$-fields and, in a broader scope, $B$-fields in high-mass star-forming regions in their earliest phases.

While dust polarization angles are useful for measuring $B$-field morphology and strengths, dust polarization fraction provides crucial constraints on dust physics (including grain alignment and disruption) and grain properties (size, shape, composition). The leading theory of grain alignment is based on radiative torques (RATs; Lazarian & Hoang 2007; Hoang & Lazarian 2016; Hoang et al. 2022). The presence of iron inclusions embedded in dust grains is predicted to enhance magnetic relaxation and increases the RAT alignment degree, aka magnetically enhanced RAT alignment or MRAT (Hoang & Lazarian 2016). The RAT theory was observationally tested in different environments, using starlight polarization (see Andersson et al. 2015 for a review) and polarized thermal dust emission in star-forming regions (Tram et al. 2021; Tram & Hoang 2022). Moreover, the RAT theory has been widely used to interpret observations such as those from Planck Collaboration et al. (2020) and Ward-Thompson et al. (2017). G11 is ideal for testing the RAT theory owing to the lack of bright embedded sources in its early phase; therefore, the only significant radiation source impacting the filament is the interstellar radiation field. In addition to that, dust polarization in the dense region can allow us to constrain grain growth (Vaillancourt et al. 2020; Hoang et al. 2021). Thus, the second aim of our paper is to probe the properties of dust grains in G11. We perform a comprehensive analysis of dust polarization fraction to constrain dust physics and dust properties. In particular, with the measured map of $B$-field strengths, it is possible to study the efficiency of magnetic relaxation and the role of the MRAT mechanism.

This paper is the first one in our series aiming at characterizing the properties of $B$-fields And dust in interstelLar fiLAments using Dust POLarization (BALLAD-POL).

The structure of the paper is as follows. In Section 2, we describe the observations and analyses of thermal dust polarization emission. Section 3 is devoted to the study of $B$-field morphology and strengths. In Section 4, we study the grain alignment physics and dust properties using the polarization fraction. Our results are discussed in Section 5. Finally, our conclusions are presented in Section 6.

## 2. Observations

In this work, we use the archival far-IR polarimetric data observed by SOFIA/HAWC+ at 214 $\mu$m wavelength toward G11 as part of the FIELDMAPS legacy project (PI: Ian W. Stephens, Worcester State University). The angular resolution is $18''.2$, corresponding to a physical scale of 0.32 pc at a distance of $\sim$3.6 kpc. G11 was mapped by mosaicking four fields of SOFIA/HAWC+. The observations were taken on 2018 July 13 with a total exposure time of 2316 s. Polarimetric observations were performed with the chop-nod imaging mode (Harper et al. 2018). We use the Level 4 data products accessible from the SOFIA archive.[10] The data reduction process was carried out using HAWC DRP PIPELINE v1.3.0 in several steps, including chop-nop subtraction, flat-field correction, flux calibration, background subtraction, polarization angle correction, and mosaic map making.

For linear polarization, the polarization states are defined by the Stokes $I$, $Q$, and $U$. The original means of signal-to-noise ratios (S/Ns) of $I$, $Q$, and $U$ are 28.3, 0.2, and 0.5, respectively. Due to the low S/Ns of the data, we binned the original $4''.55$ pixels to

$9''.1$ to increase the S/Ns. The new pixel size is about half of the beam size of SOFIA/HAWC+ at 214 $\mu$m. After binning, the mean S/Ns increase by a factor of two: 57.4 for $I$, 0.4 for $Q$, and 1.0 for $U$. Rigorous cuts will be applied to the data for further analyses that are mentioned elsewhere in the paper.

The observed intensity for each pixel is calculated by

$$PI_{\rm obs} = \sqrt{Q^2 + U^2}. \tag{1}$$

Because of the presence of the noise in $Q$ and $U$ in $PI_{\rm obs}$, we debias $PI_{\rm obs}$ by using the following relation (Serkowski 1974):

$$PI = \sqrt{Q^2 + U^2 - 0.5(\delta Q^2 + \delta U^2)}, \tag{2}$$

where the uncertainty on $PI$ is

$$\delta PI = \sqrt{\frac{Q^2 \delta Q^2 + U^2 \delta U^2}{Q^2 + U^2}}. \tag{3}$$

The polarization fraction, $P$, and its uncertainty, $\delta P$, are calculated as

$$P(\%) = 100 \times \frac{PI}{I}, \tag{4}$$

and

$$\delta P(\%) = 100 \times \sqrt{\frac{\delta PI^2}{I^2} + \frac{\delta I^2 (Q^2 + U^2)}{I^4}}. \tag{5}$$

We calculate the polarization angle, $\theta$, and its uncertainty, $\delta\theta$, by using

$$\theta = 0.5 \tan^{-1}\left(\frac{U}{Q}\right) \tag{6}$$

and

$$\delta\theta = 0.5 \times \frac{\sqrt{U^2 \delta Q^2 + Q^2 \delta U^2}}{(Q^2 + U^2)}. \tag{7}$$

The $B$-field angles on the POS are obtained by rotating the polarization angles by 90°. Following the IAU convention, the angle of $B$-fields is east of north, ranging from 0° to 180°.

For further analyses, we only use the data satisfying S/N $(I) > 10$, S/N$(P) > 3$, S/N$(\theta) > 3$, and $P < 30\%$. The resulting $B$-field orientation map is displayed in Figure 1.

To compare the $B$-field map obtained by SOFIA/HAWC+ with the one by JCMT/SCUPOL[11] (Matthews et al. 2009; Pillai et al. 2015), we plot in Figure 2 the $B$-field segments of the two observations together toward the center region, where the observations with JCMT/SCUPOL are available. The cuts applied on the JCMT/SCUPOL data are S/N$(P) > 3$, $\delta\theta < 8°$, and $P < 5\%$. There is a general agreement on the $B$-field orientation of two observations. However, the polarization fraction obtained by SOFIA/HAWC+ is significantly greater than that of JCMT/SCUPOL. The reasons for the difference could be due to the systematic of the two facilities and the dependence of polarization fraction on temperatures, densities, and dust composition (whether separate or mixed) at different wavelengths (Lee et al. 2020; Tram et al. 2021). Indeed, the shorter-wavelength emission collected by SOFIA/HAWC+ at 214 $\mu$m traces the warm dust, and the warm dust corresponds to the higher radiation field. According to the RAT theory, the
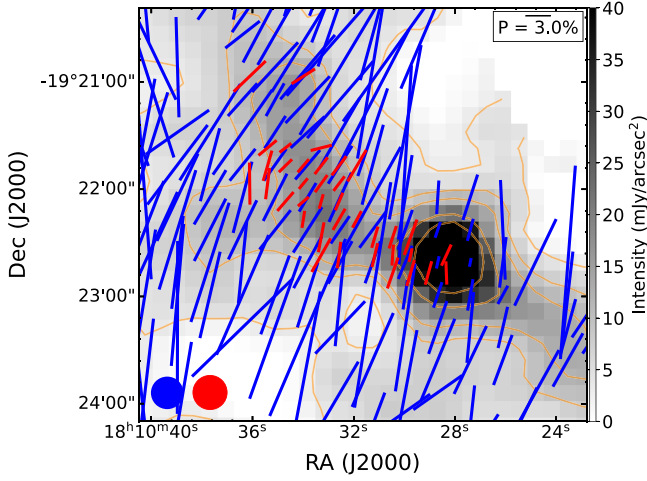
---

**Figure 2.** Comparison of the *B*-field orientation obtained by SOFIA/HAWC+ at 214 $\mu$m (blue segments) and JCMT/SCUPOL (red segments) at 850 $\mu$m. The lengths of *B*-field segments are proportional to the polarization fraction. A reference segment of 3% is given in the upper right corner. The $18''\!.2$ beam size of SOFIA/HAWC+ (blue circle) and $20''$ beam size of JCMT/SCUPOL (red circle) are shown in the lower left corner. The contours are the same as in Figure 1.

dust irradiated by a higher radiation field is better aligned with *B*-fields, i.e., higher polarization fraction, than that of the cold dust. However, this assessment is qualitative, and finding the true answer for the difference is beyond the scope of the current studies.

## 3. Magnetic Field Morphology and Strengths

### 3.1. Magnetic Field Morphology

The evolution of filament imprints on the morphology of the embedded *B*-fields. Magnetohydrodynamics simulations predict that *B*-fields are perpendicular to the filament's spine (Soler & Hennebelle 2017). We aim to quantitatively test this with G11. First, we use the filament's spine identified by *RadFil* (Zucker & Chen 2018), the magenta contour in Figure 3. A mask of the filament's column density map using a threshold $\approx 2\sigma$ above the mean background is supplied to *RalFil*. It then topologically finds the spine using medial axis skeletonization on the mask: the set of points that has more than one closest point on the mask's boundary (Koch & Rosolowsky 2015; Zucker & Chen 2018). Then, for each pixel, we find its closest point to the spine and calculate the angle difference, $\Delta\Theta$, between the *B*-field orientation angle of the pixel and the spine angle—tangent of the spine at the closest point. Figure 3 shows a map of the absolute angle differences, $|\Delta\Theta|$, indicating that the *B*-field orientations are nearly perpendicular to the spine for a major fraction of the total pixels (red pixels in the map). Figure 4 shows the dependence of $|\Delta\Theta|$ on the column densities obtained from Herschel (see Section 3.2.3). A clear tendency of the *B*-fields turning from parallel to perpendicular to the filament's spine at higher column density is present, which is consistent with the findings by Planck Collaboration et al. (2016) and Soler (2019).

### 3.2. Magnetic Field Strengths and Energy Balance of the Center Region

It was shown by Davis (1951) and Chandrasekhar & Fermi (1953) that turbulent motions generate irregular *B*-fields. Based
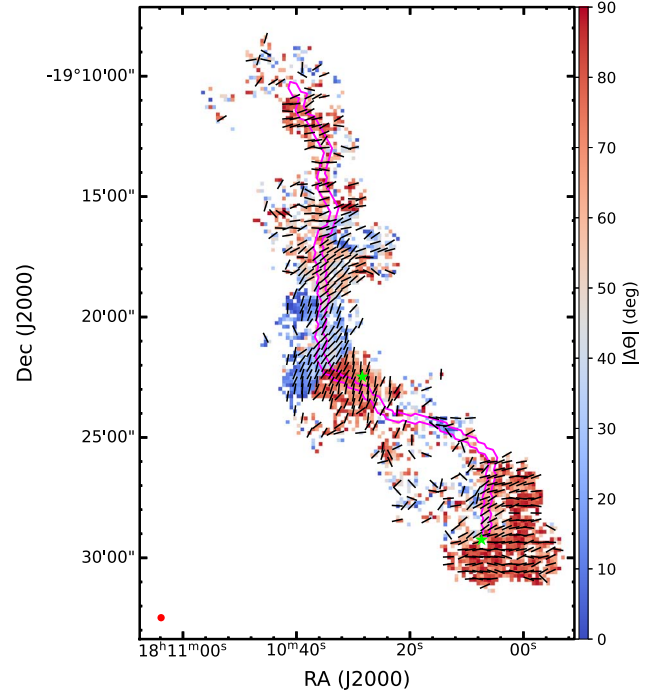


**Figure 3.** Map of the absolute angle differences between the *B*-field orientation angle and the filament's spine direction (see text). The magenta contour shows the spine. The black segments display the *B*-field orientation, with the segment length proportional to the polarization fraction of the corresponding pixel. A reference segment of 10% is given in the upper right corner of the figure. The green stars mark the locations of P1 and P6.
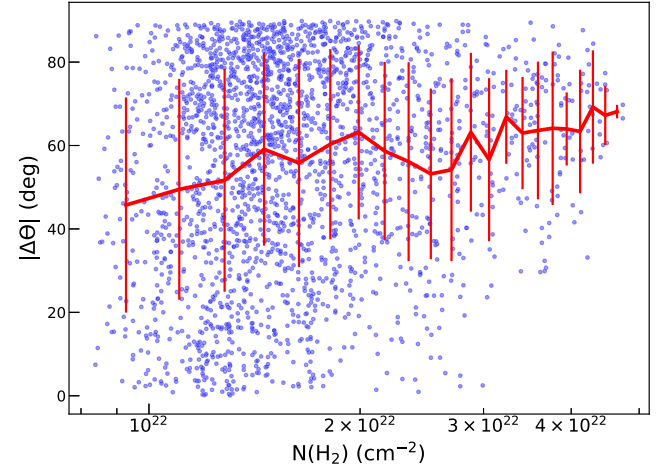


**Figure 4.** Dependence of $|\Delta\Theta|$ on column densities. The thick red curve shows the running means of $|\Delta\Theta|$, and the error bars are their rms values calculated for a bin size of $1.77 \times 10^{21}$ cm$^{-2}$.

on the analysis of the small-scale randomness of *B*-field lines, assuming that the dispersion in the *B*-field angles is proportional to the Alfvén Mach number, the *B*-field strengths can be estimated, which is called the Davis–Chandrasekhar–Fermi (DCF) method. Crutcher (2012) proposed a variant of the method, giving an estimate of the magnitude of *B*-fields in the POS, $B_{\mathrm{POS}}$, as

$$B_{\mathrm{POS}} = \mathcal{Q}\sqrt{4\pi\rho}\,\frac{\sigma_V}{\sigma_\theta} \approx 9.3\sqrt{n(\mathrm{H_2})}\frac{\Delta V}{\sigma_\theta} \quad (\mu\mathrm{G}), \qquad (8)$$

4

where $\mathcal{Q} = 0.5$ is a correction factor for line-of-sight and beam-integration effects (Ostriker et al. 2001), $\rho = \mu m_H n(H_2)$ is the gas density in $g\,cm^{-3}$ with mean molecular weight $\mu = 2.8$ and number densities $n(H_2)$ in units of $cm^{-3}$, $\sigma_V$ is the one-dimensional nonthermal velocity dispersion in $km\,s^{-1}$, $\sigma_\theta$ is the dispersion of the polarization position angles about a mean $B$-field in degrees, and $\Delta V = 2.355\sigma_V$ is the FWHM of the nonthermal velocity component in units of $km\,s^{-1}$.

To obtain a map of the $B$-field strengths using Equation (8), we generate three parameter maps for $\sigma_\theta$, $\Delta V$, and $n(H_2)$ in the following subsections.

### 3.2.1. Polarization Angle Dispersion

To calculate the polarization angle dispersion caused by the turbulent component of the $B$-fields, we apply the "un-sharp masking" method, which was first introduced by Pattle et al. (2017). Initially, the method was used to calculate the mean $B$-field strength of OMC 1 of the Orion A filament. Hwang et al. (2021) then used it to calculate the polarization angle dispersion for each pixel; therefore, they were able to obtain a map of $B$-field strengths of the same region. We first calculate the mean polarization angle, $\bar{\theta}$, in a $5 \times 5$-pixel box whose size is about two beam sizes as was done in other work such as Hwang et al. (2021) and Guerra et al. (2021). In the second step, we calculate the angle dispersion, i.e., the rms of the difference between the polarization angle of pixel $i = 1, N$ of the box, $\theta_i$, and their mean value, $\bar{\theta}$, as follows: $\sigma_\theta = \sqrt{\sum_{i=1}^{N}(\theta_i - \bar{\theta})^2/N}$. Here $N$ is the included number of pixels in the box that remain from the general cut mentioned in Section 2, which is required to be $N > 13$ ($>50\%$ of the total 25 pixels of the box). Then, we move the box and repeat the process over the whole map. Figure 5 shows the resulting map of the calculated polarization angle dispersion.

### 3.2.2. Velocity Dispersion

To build a pixel-by-pixel map of the $B$-field strengths, we need the velocity dispersion of each pixel, which requires the pixel to have high S/N and high spectral resolution to be able to fit its spectrum with a Gaussian. Archival data of sufficient quality are only available around the vicinity of the center region.

We use the $^{13}CO$ $(3 - 2)$ spectral line from the JCMT Science Archive[12] to calculate the FWHM map of the nonthermal component, $\Delta V$. Emission from CO molecules is known to trace a wide range of $H_2$ number density between $10^2$ and $10^4\,cm^{-3}$ in which $^{13}CO$ traces a moderate density of $\sim 10^3\,cm^{-3}$ (Minamidani et al. 2011; Fissel et al. 2019; Hu et al. 2019). The $^{13}CO$ $(3 - 2)$ observations toward the center of G11 were carried out as part of the JCMT observations (proposal ID M15AI41). These observations were made on 2015 April 2 using the HARP instrument tuned to the central frequency of 330.587 GHz with a total integration time of 1675 s and atmospheric opacity ranging from 0.039 to 0.047 at 225 GHz. The data were reduced by using the ORAC Data Reduction (ORAC-DR) pipeline (Buckle et al. 2009) and the Kernel Application Package (KAPPA; Currie et al. 2014) in Starlink. The original spectral resolution of the data set is 0.055 $km\,s^{-1}$. The spectra are smoothed to have the final resolution of 0.2 $km\,s^{-1}$. The spectrum of each pixel is then fitted to a
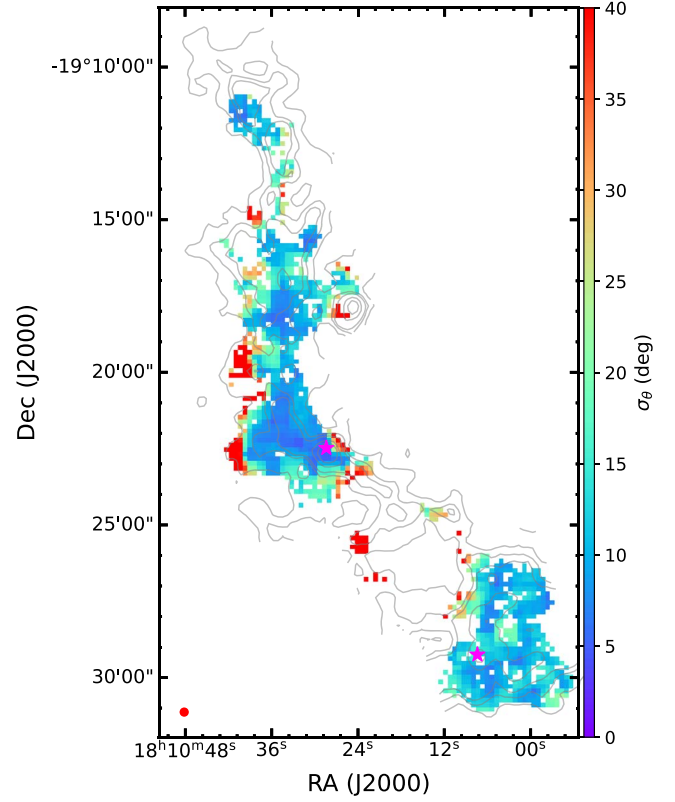
**Figure 5.** The polarization angle dispersion map of G11. The contours are the same as in Figure 1.
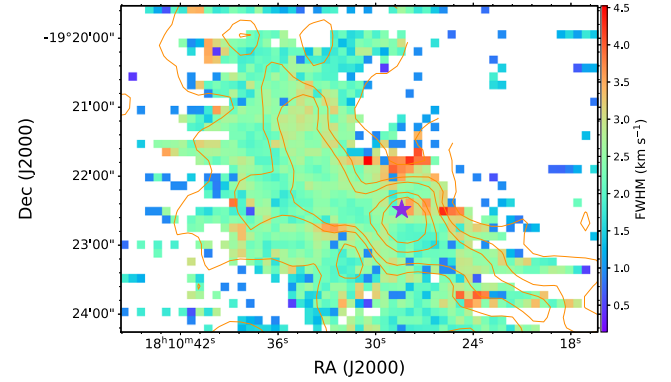


**Figure 6.** The FWHM map of the nonthermal component obtained from $^{13}CO$ spectral lines for the center region. The contours are the same as in Figure 1. The star marker shows the location of P1.

Gaussian using *fit1d* of the SMURF package (Chapin et al. 2013) to obtain the FWHM map of $^{13}CO$ $(3 - 2)$, $\Delta V^2_{total,\,^{13}CO}$.

The nonthermal velocity component, $\Delta V$, is calculated using $\Delta V^2 = \Delta V^2_{total,\,^{13}CO} - \frac{k_B T}{m_{^{13}CO}} 8 \ln 2$, where $m_{^{13}CO} = 29\,amu$ is the molecular mass of $^{13}CO$, $k_B$ is the Boltzmann constant, and $T$ is the gas temperature. The thermal contribution to the velocity dispersion is negligible if we adopt an average gas temperature of 20 K. We show the map of the nonthermal velocity dispersion of the central region in Figure 6.

### 3.2.3. Volume Densities

For calculating the volume densities, we use the maps of the column densities, $N(H_2)$, and dust temperatures, $T_d$, derived by
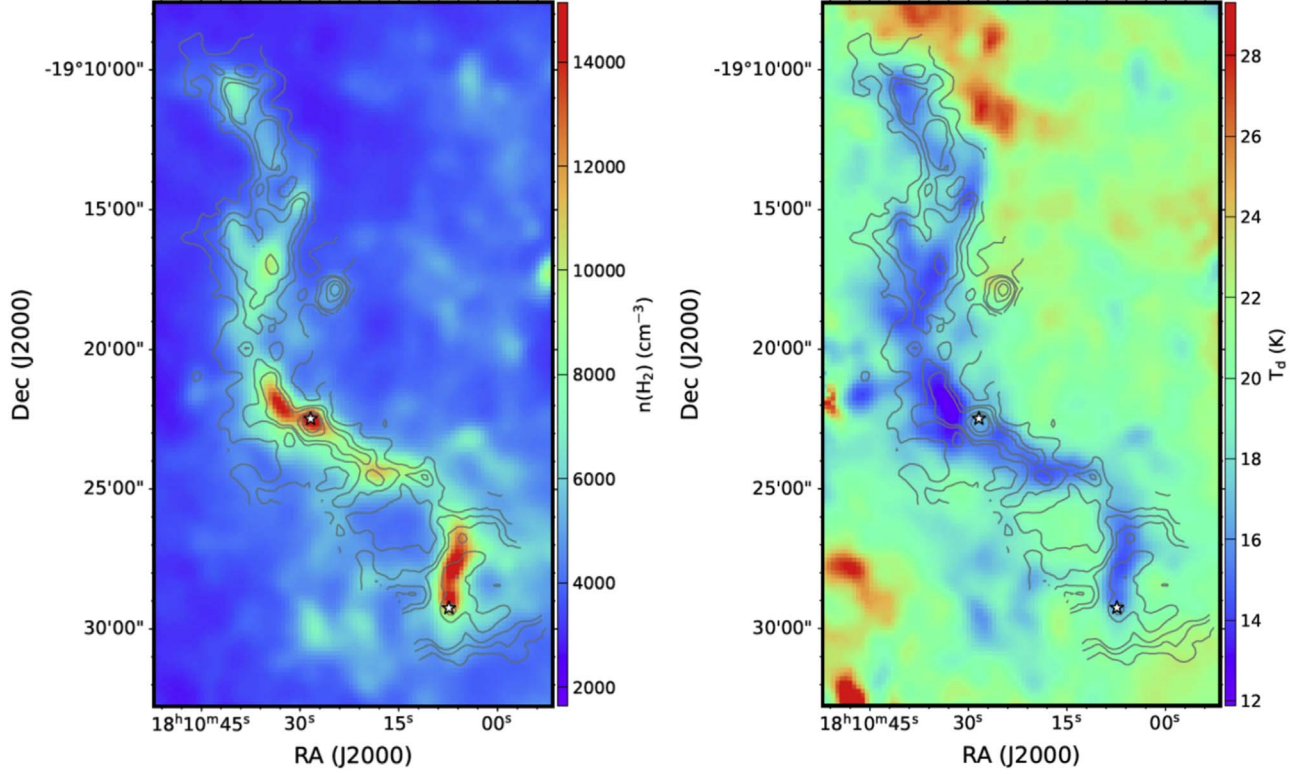
**Figure 7.** Maps of the volume densities (left) and dust temperatures (right) of G11. Contours are the same as in Figure 1.

Zucker et al. (2018) from the multiwavelength Herschel data. The resolution of these maps is $43''$ ($\sim 1.4$ pc) with a pixel size of $11{.}''5 \times 11{.}''5$. Zucker et al. (2018) also fitted the spine of G11 using the *RadFil* algorithm (Zucker & Chen 2018) and found that the filament has a length of 22 pc and a width of 1.0 pc. We assume that the filament has a cylindrical shape so that the depth of the filament is equal to its width. The volume densities can then be calculated as follows:

$$n(\mathrm{H_2}) = \frac{N(\mathrm{H_2})}{W}, \tag{9}$$

where $W$ is the depth equal to 1.0 pc. The maps of $n(\mathrm{H_2})$ and $T_d$ are shown in Figure 7. The volume densities are in the range of $10^3$–$10^5$ cm$^{-3}$.

### 3.2.4. Magnetic Field Strengths

We use Equation (8) to calculate the $B$-field strength for each pixel with polarization angle dispersion, $\sigma_\theta$, smaller than $25°$, as suggested by Ostriker et al. (2001). Figure 8 shows the map of $B$-field strengths toward the center region. The strengths vary from $100\,\mu$G in the outer region to $\sim 600\,\mu$G in the filament's spine with a mean value of $235\,\mu$G.

Mapping the $B$-field strengths has been done only for a few objects: Orion A (Guerra et al. 2021; Hwang et al. 2021), Monoceros R2 (Hwang et al. 2022), and 30 Doradus (Tram et al. 2023). Before these studies, the mean values of $B$-field strengths were only estimated. Therefore, to test the robustness of the obtained $B$-field strengths for G11, we also use the structure function method (Hildebrand et al. 2009) as was done in our previous work (Ngoc et al. 2021; Thuong et al. 2022) to calculate the mean $B$-field strength for the center region. The polarization angle dispersion obtained with the structure function method is $\sigma_\theta = 10{.}°5 \pm 4{.}°6$. The mean number density
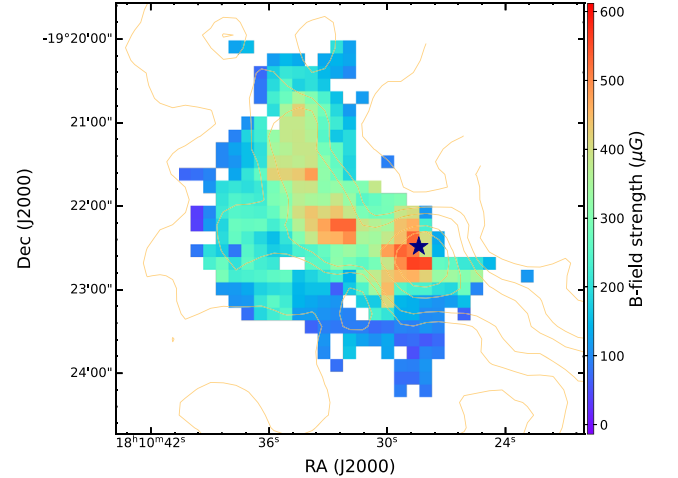


**Figure 8.** Map of $B$-field strengths calculated for each pixel toward the center region of G11. The violet star indicates the location of the massive protostellar candidate (P1). The contours are the same as in Figure 1.

and nonthermal velocity dispersion are $n(\mathrm{H_2}) = (8.0 \pm 1.4) \times 10^3$ cm$^{-3}$ and $\Delta V = 2.4 \pm 0.4$ km s$^{-1}$, respectively. Putting these values to Equation (8), we obtain the mean value of $B_{\mathrm{POS}} = 242 \pm 50\,\mu$G. This value lies well in the range of the $B$-field strengths calculated on the pixel-to-pixel basis, which ensures the mapping process's quality.

### 3.2.5. Mass-to-flux Ratios

The relative importance of gravity to $B$-fields is usually described by the mass-to-flux ratio, $M/\Phi$. In the units of the critical value, the mass-to-flux ratio is given by the following
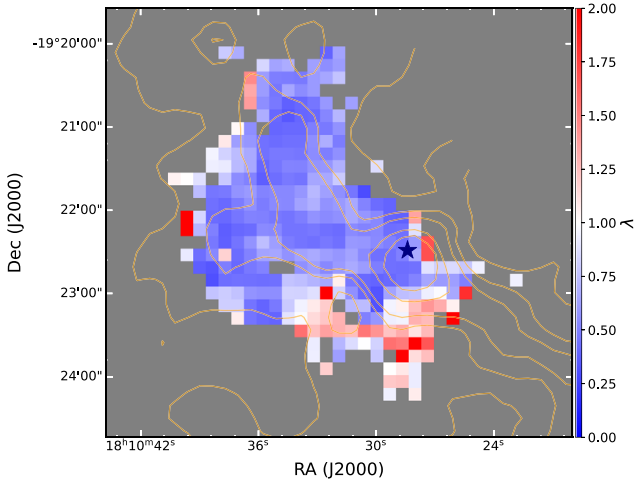
**Figure 9.** Map of mass-to-flux ratio toward the center region of G11. The violet star is the location of the massive protostellar candidate (P1). The contours are the same as in Figure 1.

relation (Crutcher 2004):

$$\lambda = \frac{(M/\Phi)_{\text{observed}}}{(M/\Phi)_{\text{critical}}} = 7.6 \times 10^{-21} \frac{N(\text{H}_2)}{B_{\text{tot}}}, \qquad (10)$$

where $(M/\Phi)_{\text{critical}} = 1/(2\pi\sqrt{G})$, $G$ is the gravitational constant, $N(\text{H}_2)$ is measured in cm$^{-2}$, and $B_{\text{tot}}$ is the total $B$-field strength in $\mu$G, which is approximated to be $B_{\text{tot}} = 1.3 \times B_{\text{POS}}$ (Crutcher 2004).

Figure 9 shows a map of the mass-to-flux ratio toward the central region in which blue represents $\lambda < 1$ and red represents $\lambda > 1$. It is visible that most of the region is subcritical, meaning that the gravity is not strong enough for the gravitational collapse to occur to form new stars. This is consistent with the scenario that the filament is in its early phase, accreting material from the outer region onto the filament's spine following the $B$-field lines. The southwestern part of the considered region is supercritical, which is close to the location of the massive protostellar candidate P1 (violet star marker).

### 3.2.6. Alfvén Mach Number

The interplay between the $B$-fields and turbulence can be evaluated by the Alfvén Mach number. The Alfvénic Mach number, $\mathcal{M}_A$, of the gas is given by

$$\mathcal{M}_A = \frac{\sigma_V}{\nu_A}, \qquad (11)$$

where $\sigma_V$ is the one-dimensional nonthermal velocity dispersion and $\nu_A = B_{\text{tot}}/\sqrt{4\pi\rho} = \mathcal{Q} \times \sigma_V/\sigma_\theta$ is the Alfvénic velocity; both $\sigma_V$ and $\nu_A$ are measured in km s$^{-1}$. Combining Equation (11) and $\nu_A$, we have $\mathcal{M}_A = \sigma_\theta/\mathcal{Q}$. As mentioned earlier, we take the correction factor $\mathcal{Q} = 0.5$, and $\sigma_\theta$ is now in radian. Equation (8) is equivalent to $\mathcal{M}_A \approx 3.5 \times 10^{-2}\sigma_\theta$, where $\sigma_\theta$ is measured in degrees (Pattle et al. 2021).

Since the Alfvén Mach number depends only on the polarization angle dispersion, we produce a map of the Alfvén Mach number for the whole Snake filament (Figure 10). The color scale of the map is such that blue represents $\mathcal{M}_A < 1$ and red represents $\mathcal{M}_A > 1$. The overall color of the map is blue; therefore, the region is mostly sub-Alfvénic. Only the
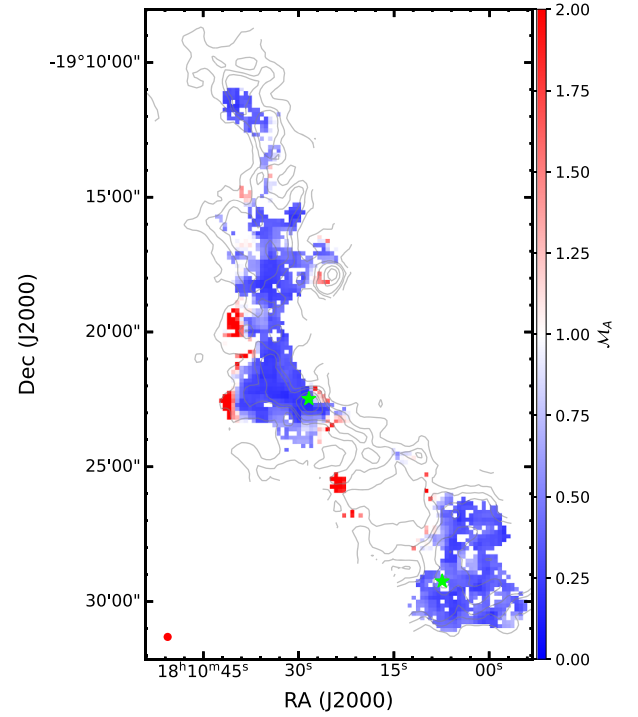


**Figure 10.** Map of Alfvén Mach number. The violet stars mark the locations of the massive protostellar candidates (P1 and P6). The contours are the same as in Figure 1.

outermost regions of the filament from its spine are found to be trans- or super-Alfvénic. The energy of the $B$-fields is dominated over that of the nonthermal motions. Once again, the results are in line with the ordered $B$-field morphology observed in the filament. The impact of the gas turbulence is not strong enough, and the $B$-fields are able to regulate the gas motion.

## 4. Dust Physics and Grain Properties

In this section, we perform various analyses using the polarization fraction to study grain alignment physics and dust grain properties in G11. First, we analyze the relation of the obtained polarization fraction, $P$, with the intensities, $I$, gas column densities, $N(\text{H}_2)$, and dust temperatures, $T_d$.

### 4.1. Maps of Gas Densities and Dust Temperatures

Gas densities and dust temperatures are the key parameters of the grain alignment mechanism based on RATs. We use the H$_2$ column densities and dust temperatures produced by Zucker et al. (2018) using modified blackbody fitting to the data from Herschel's four bands at 160, 250, 350, and 500 $\mu$m.

Figure 7 shows the maps of gas densities (left) and dust temperatures (right). The dust temperatures decrease from $T_d > 20$ K in the diffuse region to $T_d \lesssim 15$ K close to the filament's spine. This reveals that dust grains inside the filament are heated only by the interstellar radiation field and that the contribution of the internal radiation from protostellar candidate sources P1 and P6 is subdominant.

### 4.2. Polarization Fraction Map

Figure 11 displays a $B$-field orientation map similar to Figure 1, but the segment lengths are now proportional to the
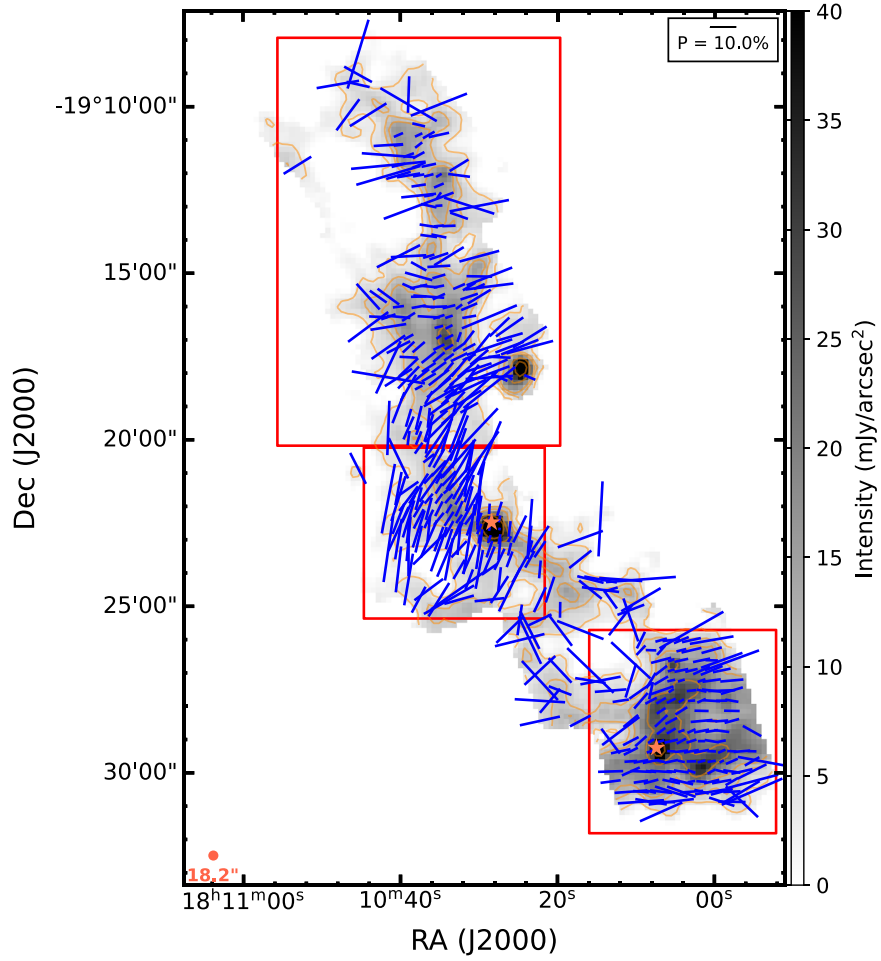
**Figure 11.** Same as Figure 1, but the length of polarization vectors now represents the polarization fraction. Three regions mentioned in the text are defined by the three red rectangles for the North, Center, and South regions, respectively.

polarization fraction, $P$. For further studies, we divide the filament into three subregions, North, Center, and South, represented by the three red rectangles in Figure 11. We note that the newly defined Center region (Center with capital C) is slightly different from the center region encompassed by a circle shown in Figure 1 in previous sections, which overlaps with the observed region of JCMT/SCUPOL. It is clearly seen that the polarization fraction is higher in the more diffuse regions far from the filament's spine but drops significantly in the regions close to the filament's spine, where the thermal emission intensities are higher. This effect, called "depolarization" or "polarization hole," is a common phenomenon that has been reported by both optical−near-IR (Whittet et al. 2008) and far-IR/submillimeter observations (e.g., Ward-Thompson et al. 2000) toward molecular clouds. The origin of the depolarization effect is still under debate (e.g., Pattle & Fissel 2019; Hoang et al. 2021)

Figure 12 shows the histograms of the polarization fraction. The mean polarization fraction for the three regions is about 10%, but there are many pixels with high polarization above 20%. The Center region appears to have a higher polarization fraction than that of the North and South regions.

### 4.3. Polarization Fraction versus Total Intensities

Figure 13 displays the variation of $P$ with $I$. The polarization fraction is very high ($\sim$10%–30%) in the outer regions with
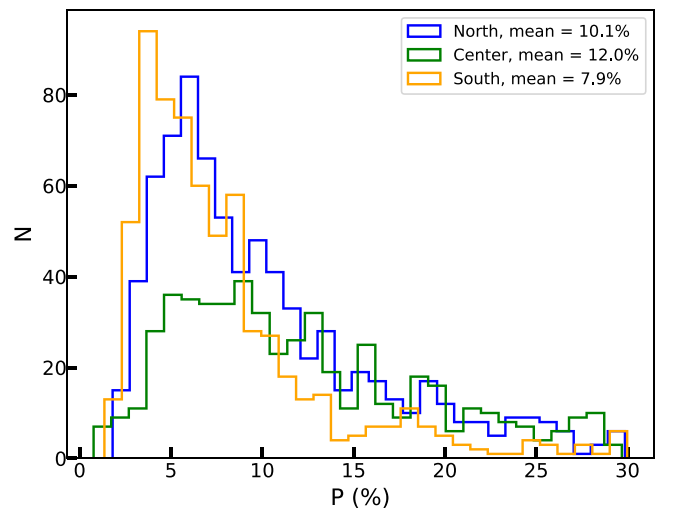


**Figure 12.** Distributions of the polarization fractions of North (blue), Center (green), and South (orange).

intensities $I < 8$ (mJy arcsec$^{-2}$), but it decreases with increasing total intensities toward the filament's spine. Power-law fits to this variation of the form $P \propto I^{-\alpha}$ give the power indices $\alpha = 0.93 \pm 0.02$, $0.81 \pm 0.02$, and $0.80 \pm 0.02$ for the North, Center, and South regions, respectively. The uncertainties on $\alpha$
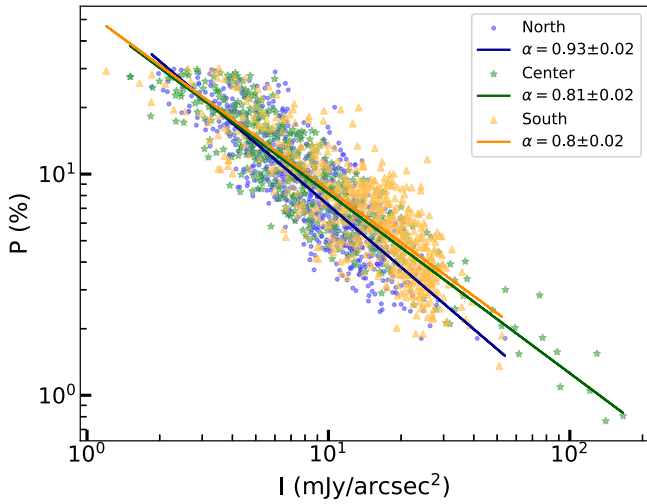
**Figure 13.** Dependence of polarization fraction, $P(\%)$, on intensity, $I$, observed by SOFIA/HAWC+ for North (blue), Center (green), and South (orange). Solid lines show the power-law fit to the data. The slope of the North region is steeper than that of the Center and South regions.

are only statistical and the result of the fits. We note that the value of $\alpha$ is an indication of the variation of the grain alignment efficiency and the $B$-field tangling along the line of sight. In general, the expected values of $\alpha$ for molecular clouds or cores are between 1 and 0. The index $\alpha = 1$ indicates a near-total lack of alignment in dense regions usually found for starless-core clouds, and a shallower slope with $\alpha < 1$ implies that grains are still aligned in the inner regions of the cloud (Hoang et al. 2022). In particular, the slope with $\alpha = 0.5$ can be reproduced with a model of uniform grain alignment with supersonic and sub-Alfvénic turbulence (Falceta-Gonćalves et al. 2008). Turbulence is the main source of field tangling (Jones 1989; Jones et al. 1992; Falceta-Gonćalves et al. 2008).

We found slopes of $\alpha \sim 0.8$ for the Center and South regions, which are shallower than that of the North ($\alpha \sim 0.9$). This means that grain alignment in the Center and South regions is more efficient than in the North. Interestingly, there exist two massive star candidates P1 and P6 in the Center and South regions, which may contribute to inducing grain alignment in the inner regions and making the slopes shallower (Hoang et al. 2021). The slopes of $\alpha < 1$ suggest that grain alignment is not entirely lost. We discuss the implication of found slopes and provide evidence for grain growth in the filament in Section 5.4.

### 4.4. Polarization Fraction versus Column Densities and Dust Temperatures

The grain alignment efficiency depends on the local conditions, including the radiation field and gas densities, according to the RAT theory (Hoang et al. 2021). To study clearly how the local conditions of G11 affect the dust polarization fraction, in Figure 14 we plot the relation of $P$ to the column densities (left panel) and dust temperatures (right panel).

The $P - N(\mathrm{H_2})$ relation shows an anticorrelation that can be described by a power-law model of the form $P \propto N(\mathrm{H_2})^{-\alpha_N}$ with slopes $\alpha_N = 1.54 \pm 0.08$ for North, $\alpha_N = 1.37 \pm 0.05$ for Center, and $\alpha_N = 0.93 \pm 0.06$ for South. Similar to the $P - I$ relation, the slope $\alpha_N$ for the North region is steeper than that for the Center and South regions, which implies the role of two

massive star candidates P1 and P6 in the enhanced alignment in the latter regions.

The $P - T_d$ relation shows the correlation of the polarization fraction and the dust temperatures or equivalent to the radiation field strength. A power-law fit of the form $P \propto T_d^{\alpha_T}$ to the observational data yields the slopes $\alpha_T = 2.16 \pm 0.17$ for North, $\alpha_T = 2.5 \pm 0.24$ for Center, and $\alpha_T = 2.04 \pm 0.18$ for South. A detailed discussion on the grain alignment physics using these results is presented in Section 4.6.

### 4.5. Magnetic Field Tangling

In addition to grain alignment and dust grain properties, polarization fraction, $P$, also depends on the $B$-field geometry along the line of sight. To disentangle the effect of $B$-field tangling and grain alignment on the observed dust polarization, we now analyze the polarization angle dispersion function, $\mathcal{S}$, and the product $P \times \mathcal{S}$. The product $P \times \mathcal{S}$ describes the averaged alignment efficiency of grains along the line of sight (Planck Collaboration et al. 2020). This implication is based on the observation that, for a constant grain alignment efficiency, the larger/smaller $\mathcal{S}$ would imply stronger/weaker $B$-field tangling, which produces a smaller/larger polarization fraction. Therefore, the product $P \times \mathcal{S}$ would provide us with information about the overall grain alignment.

We first calculate $\mathcal{S}$ using the definition described in Section 3.3 of Planck Collaboration et al. (2020). For each pixel at location $x$, $\mathcal{S}(x)$ is calculated as the rms of the polarization angle difference, $\mathcal{S}_{xi}$, of the considered pixel $x$ and pixel $i$ lying on a circle having $x$ as the center and a radius of $\delta$:

$$\mathcal{S}^2(x) = \frac{1}{N}\sum_{i=1}^{N}\mathcal{S}_{xi}^2, \qquad (12)$$

where $\mathcal{S}_{xi} = \theta(x) - \theta(x + \delta)$ is the polarization angle difference and $N$ is the number of pixels lying on the circle. For the current study, we calculate $\mathcal{S}(x)$ for $\delta$ equal to two times the beam size of SOFIA/HAWC+.

Due to noise on the Stokes parameters $Q$ and $U$, $\mathcal{S}$ is biased. The bias of $\mathcal{S}$ can be positive or negative depending on whether the true value is smaller or larger than the random polarization angle $52°$ (Alina et al. 2016).

The variance of angle dispersion function, $\sigma_\mathcal{S}$, and the debiased $\mathcal{S}$ is calculated as (see Section 3.5 of Planck Collaboration et al. 2020)

$$\sigma_\mathcal{S}(x) = \frac{\delta\theta(x)}{N^2\mathcal{S}^2}\left(\frac{1}{N}\sum_{i=1}^{N}\theta(x + \delta) - \theta(x)\right)^2$$
$$+ \frac{1}{N^2\mathcal{S}^2}\sum_{i=1}^{N}\delta\theta^2(x + \delta)(\theta(x + \delta) - \theta(x))^2 \qquad (13)$$

and

$$\mathcal{S}_{\mathrm{db}}^2(x) = \mathcal{S}^2(x) - \sigma_\mathcal{S}(x)^2, \quad \text{if } \mathcal{S} > \sigma_\mathcal{S}, \qquad (14)$$

where $\sigma_\mathcal{S}(x)$ is the variance of $\mathcal{S}(x)$. Hereafter, we refer to $\mathcal{S}_{\mathrm{db}}(x)$ as $\mathcal{S}$ for convenience.

Figure 15 (left) shows the relation of $P$ versus $\mathcal{S}$ calculated for three different regions. The solid lines show the running means of the polarization fraction. The polarization fraction does not exhibit a clear variation with $\mathcal{S}$, although the data are scattered. However, in Figure 15 (right) we show $P \times \mathcal{S}$ versus $I$, which exhibits a steep decrease of $P \times \mathcal{S}$, i.e., the observed
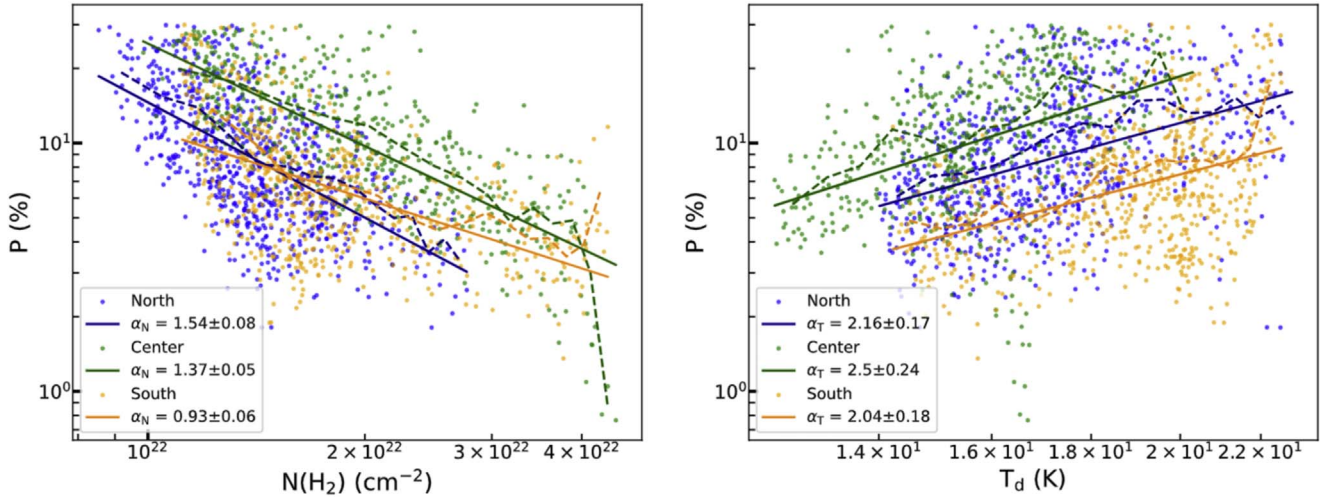
**Figure 14.** Dependence of polarization fraction, $P(\%)$, on column densities, $N(H_2)$ (left), and dust temperatures, $T_d$ (right). Solid lines are the results of the fits to a power-law function (see text). The dashed lines show the mean values calculated per bin size of $1.3 \times 10^{21}$ cm$^{-2}$ for $N(H_2)$ and 0.6 K for $T_d$.
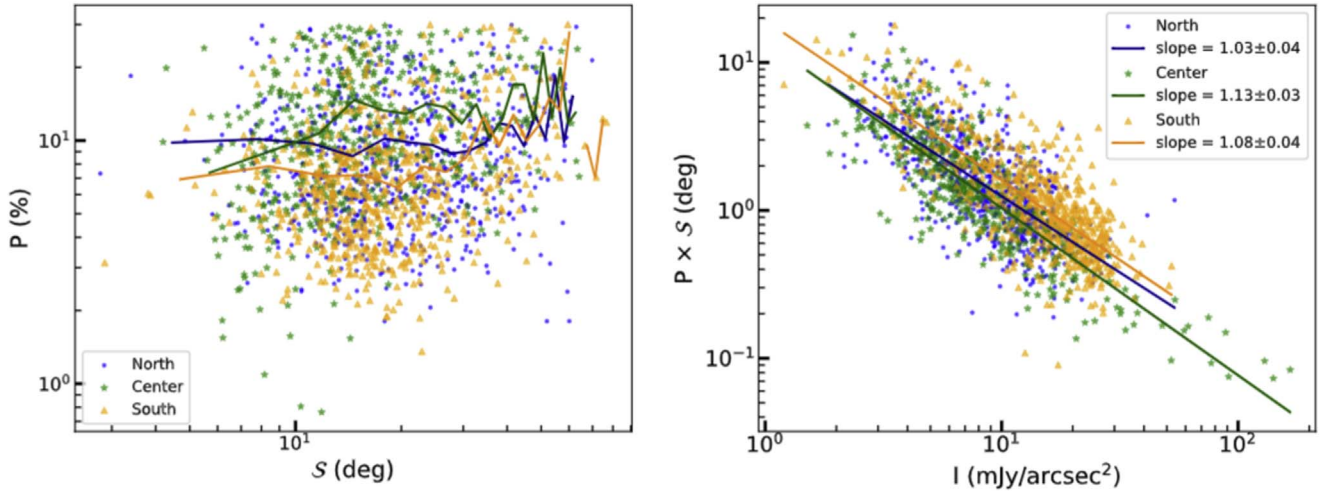


**Figure 15.** Left: dependence of polarization fraction, $P(\%)$, on polarization angle dispersion function, $\mathcal{S}$. The solid curves show the running means. Right: the variation of $P \times \mathcal{S}$ vs. $I$. Dashed curves show the running means, and the solid lines are the results of power-law fits (see text).

alignment efficiency, with increasing $I$. Thus, the dominant cause of the depolarization in G11 is not the $B$-field tangling but the decrease of grain alignment efficiency.

### 4.6. Grain Alignment Mechanisms

We now apply the modern theory of grain alignment to understand the observed dust polarization fraction and various analyses shown in the previous section.

According to the RAT theory, grains are effectively aligned only when they can rotate suprathermally, i.e., a rotation rate much higher than the thermal value (Hoang & Lazarian 2008, 2016). The minimum size of aligned grains, hereafter alignment size, can be calculated by the following formula (Hoang et al. 2021):

$$a_{\text{align}} \simeq 0.055 \hat{\rho}^{-1/7} \left( \frac{\gamma U}{0.1} \right)^{-2/7} \left( \frac{n_H}{10^3 \text{ cm}^{-3}} \right)^{2/7}$$

$$\times \left( \frac{T_{\text{gas}}}{10 \text{ K}} \right)^{2/7} \left( \frac{\bar{\lambda}}{1.2 \ \mu\text{m}} \right)^{4/7} (1 + F_{\text{IR}})^{2/7}, \quad (15)$$

where $\hat{\rho} = \rho_d/(3 \text{ g cm}^{-3})$, with $\rho_d$ the dust mass density; $\gamma$ is the anisotropy degree of the radiation field; $\bar{\lambda}$ is the mean wavelength; and $U$ is the strength of the radiation field. Above, $n_H$ is the number density of hydrogen atoms, $T_{\text{gas}}$ is the gas temperature, and $F_{\text{IR}}$ is the ratio of the IR damping to the collisional damping rate. As shown in Equation (15), the alignment size increases with increasing gas density, but it decreases with increasing radiation strength, $U$ (or dust temperature).

Within the RAT paradigm, the dust polarization fraction is determined by the size distribution of aligned grains, spanning from $a_{\text{align}}$ to the maximum grain size, $a_{\text{max}}$ (Hoang & Lazarian 2014; Lee et al. 2020). The latter value is determined by grain growth and destruction processes. For a given $a_{\text{max}}$, a larger value of $a_{\text{align}}$ results in a narrower size distribution of aligned grains, which produces a lower polarization fraction, $P$. Similarly, a smaller value of $a_{\text{align}}$ causes the higher $P$ because of the wider size distribution of aligned grains (see Tram & Hoang 2022).
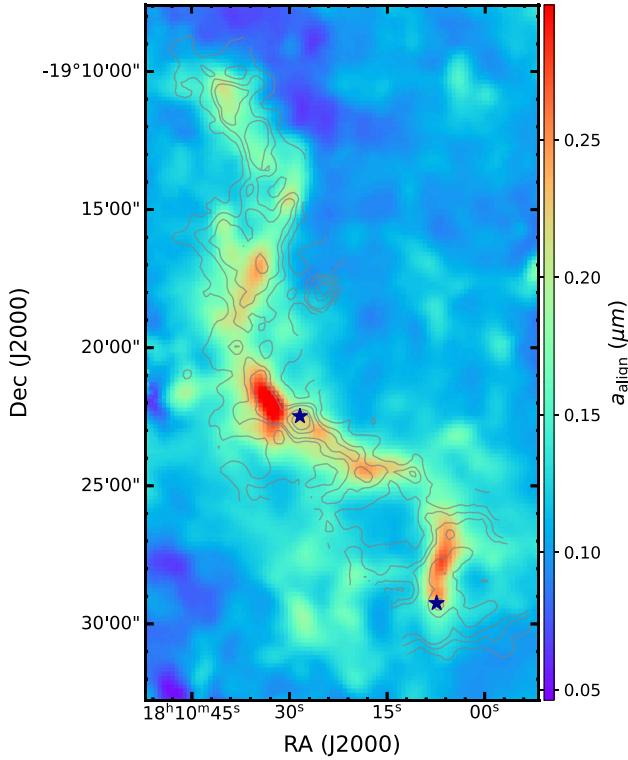
**Figure 16.** Map of alignment sizes calculated within the framework of RATs, $a_{\mathrm{align}}$. The alignment size increases from the outer to the inner region of the filament.



**Figure 17.** Variation of the alignment size, $a_{\mathrm{align}}$, with intensity, $I$. The dashed lines show the running mean values. Solid curves are the power-law fits to the data for the three regions.

For calculations of alignment size in G11, we assume the local radiation field of $\gamma = 0.1$, $\bar{\lambda} = 1.2\ \mu$m, $T_{\mathrm{gas}} = T_d$ (thermal equilibrium assumption between gas and dust is valid for dense and cold environments). The anisotropy degree of radiation $\gamma = 0.1$ is typical for the diffuse interstellar radiation field (Draine & Weingartner 1997; Bethell et al. 2007). G11 has no nearby bright star, and the dust is mainly heated by the interstellar radiation field; therefore, $\gamma = 0.1$ is chosen. We use $T_d$ and $n_{\mathrm{H}} = 2n(\mathrm{H}_2)$ maps of G11 shown in Figure 7. To obtain $U$, we use the relationship between the dust temperature and the radiation strength for silicate grains having sizes in the range of $0.01$–$1\ \mu$m with dust heating and cooling balance and radiation strength $U < 10^4$ ($\sim$75 K): $U \approx (T_d/16.4\ \mathrm{K})^6$ (Draine 2010).

Figure 16 shows the map of the alignment sizes. The alignment sizes increase from the outer layer to the filament's spine as a consequence of the increase of the gas density and the decrease of the dust temperature (see Figure 7). Compared to the map of the polarization fraction (see Figure 11), one can see the overall anticorrelation of $a_{\mathrm{align}}$ and $P$ as expected.

Upon closer inspection of the variation of the polarization fraction on the alignment size, we plot the variation of $a_{\mathrm{align}}$ with $I$ in Figure 17. The alignment size increases with the intensity, with slightly shallower slopes for the Center and South regions.

Figure 18 shows the variation of $P$ (left) and $P \times \mathcal{S}$ (right) with $a_{\mathrm{align}}$. The decrease in polarization fraction and alignment efficiency is visible with increasing the alignment size by RATs. From numerical modeling, it is found that, as $a_{\mathrm{align}}$ increases, the polarization fraction decreases owing to the reduction of the fraction of aligned grains (Lee et al. 2020; Hoang et al. 2021). Hence, the depolarization in G11 could be explained by the decrease in the RAT alignment efficiency
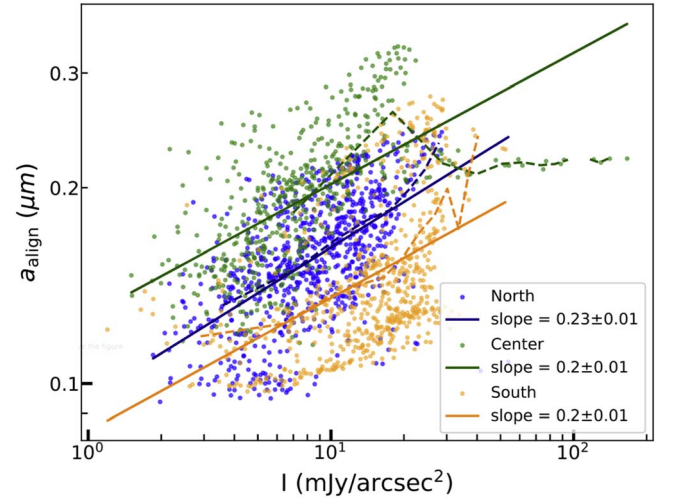
toward the high column density with low dust temperature regions.

### 4.7. Magnetic Relaxation

The magnetic properties of dust are essential for their interaction and alignment with the ambient $B$-fields. Dust grains containing embedded iron atoms make interstellar dust a natural paramagnetic material. Dust grains become superparamagnetic when iron atoms are distributed as clusters inside the grains (e.g., Hoang et al. 2022). The alignment of the grain angular momentum with the $B$-fields is usually thought to be due to paramagnetic relaxation (Davis & Greenstein 1951). Nevertheless, the paramagnetic relaxation alone cannot produce efficient alignment and is insufficient to explain the observational data (Hoang & Lazarian 2016). In the presence of RATs, magnetic relaxation, the general case of relaxation due to magnetic dissipation for any type of magnetic material (para, super-para, ferro-magnetic, etc.), can enhance the alignment degree, known as magnetically enhanced RAT (or MRAT) alignment mechanism (Hoang & Lazarian 2016).

The strength of magnetic relaxation, $\delta_{\mathrm{mag}}$, is defined by the ratio of the gas collision damping timescale, $\tau_{\mathrm{gas}}$, to magnetic relaxation time, $\tau_{\mathrm{mag,sp}}$. For grains with embedded iron clusters that are plausible for grains in dense regions due to grain evolution, one has

$$\delta_{\mathrm{mag,sp}} = \frac{\tau_{\mathrm{gas}}}{\tau_{\mathrm{mag,sp}}} = 56 a_{-5}^{-1} \frac{N_{cl} \phi_{\mathrm{sp},-2} \hat{p}^2 B_3^2}{\hat{\rho} n_4 T_{\mathrm{gas},1}^{1/2}} \frac{k_{\mathrm{sp}}(\Omega)}{T_{d,1}},\qquad (16)$$

where $a_{-5} = a/(10^{-5}\ \mathrm{cm})$; $B_3 = B_{\mathrm{tot}}/(10^3\ \mu\mathrm{G})$; $n_4 = n_{\mathrm{H}}/(10^4\ \mathrm{cm}^{-3})$, with $n_{\mathrm{H}} \approx 2n(\mathrm{H}_2)$ for molecular gas; $T_{\mathrm{gas},1} = T_{\mathrm{gas}}/(10\ \mathrm{K})$; $T_{d,1} = T_d/(10\ \mathrm{K})$; $\hat{p} = p/5.5$, with $p \approx 5.5$ the coefficient describing the magnetic moment of an iron atom; $N_{\mathrm{cl}}$ is the number of iron atoms per cluster; $\phi_{\mathrm{sp}}$ is the volume filling factor of iron clusters with $\phi_{\mathrm{sp},-2} = \phi_{\mathrm{sp}}/0.01$; and $k_{\mathrm{sp}}(\Omega)$ is the function of the grain rotation frequency $\Omega$, which is of order unity (see Hoang et al. 2022 for details).

Magnetic relaxation is considered effective when $\delta_{\mathrm{mag,sp}} > 1$, i.e., relaxation occurs faster than the gas rotational damping. Numerical calculations in Hoang & Lazarian (2016) show that
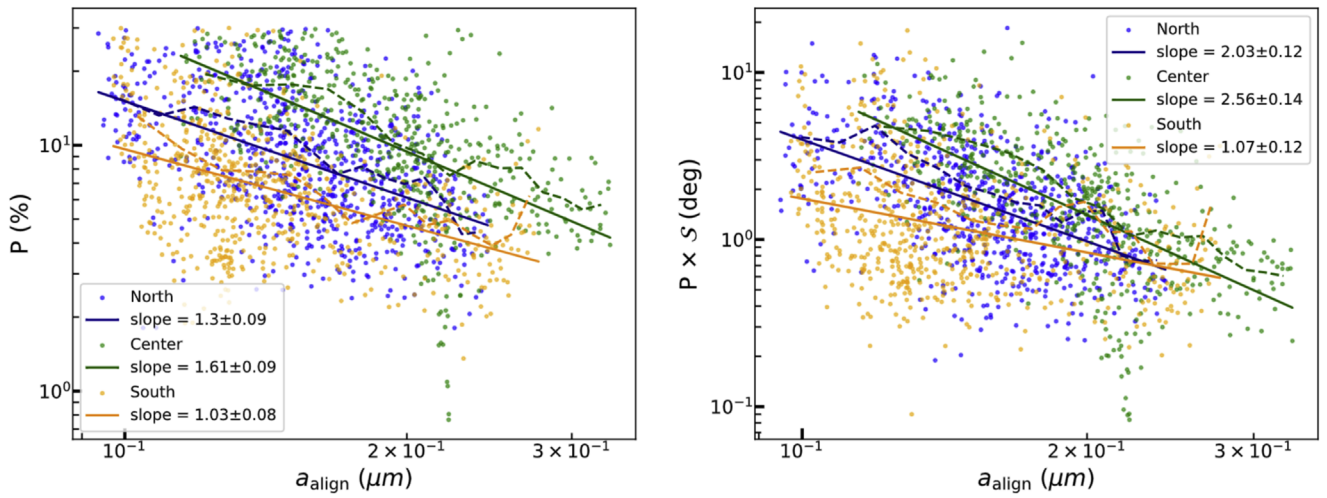
**Figure 18.** The variation of the polarization fraction (left) and of the alignment efficiency, $P \times S$ (right), on the alignment size, $a_{\mathrm{align}}$. The dashed lines show the running means, and solid lines are the results of the fits to a power-law function (see text).

the joint action of suprathermal rotation by RATs and magnetic relaxation can enhance the alignment degree so that superparamagnetic grains can achieve perfect alignment for $\delta_{\mathrm{mag,sp}} > 10$.

To study whether magnetic relaxation has any effects on RAT alignment in this filament, we use the maps of the gas densities, $n_{\mathrm{H}}$, $B$-field strengths, $B_{\mathrm{tot}}$, and dust temperature, $T_d$, and plug their values into Equation (16) to obtain $\delta_{\mathrm{mag,sp}}$ for the entire filament. We assume the typical value of $N_{\mathrm{cl}} = 100$ and $\phi_{\mathrm{sp}} = 0.01$ (i.e., about 3% of iron abundance in the form of iron clusters; see Hoang & Lazarian 2016). Figure 19 shows the results. As shown, even for the chosen parameters with a low level of iron inclusions, one has $\delta_{\mathrm{mag,sp}} \gtrsim 10$ in the entire filament, indicating that magnetic relaxation is very efficient in the filament, so that grains can achieve perfect alignment owing to the MRAT mechanism (Hoang et al. 2022). More discussions on magnetic relaxation in the region are presented in Section 5.3.

Finally, we note that although $\delta_{\mathrm{mag,sp}}$ increases toward the inner region of the filament (see Figure 19), the expected polarization degree does not necessarily increase because of the saturation of MRAT alignment efficiency and the increase in the minimum alignment size $a_{\mathrm{align}}$ (see the previous subsection).

## 5. Discussions

### 5.1. Characteristics of B-fields and Comparison with Previous Studies

$B$-fields are thought to play an important role in the formation and evolution of interstellar filament and the regulation of star formation (McKee & Tan 2003; Henney et al. 2009). Previous studies have revealed that $B$-fields tend to be parallel to the filament in the diffuse regions of low column densities, and they become perpendicular to the filament in dense regions of high column density with $N_{\mathrm{H}} \gtrsim (3\text{–}5) \times 10^{21}\,\mathrm{cm}^{-2}$ (Planck Collaboration et al. 2016; Soler & Hennebelle 2017; Soler et al. 2017).

In this paper, we derived the $B$-field orientation map by using polarimetric data taken by SOFIA/HAWC+. We found that the $B$-fields in G11 are mostly perpendicular to the filament's spine, in particular at the highest column densities (see
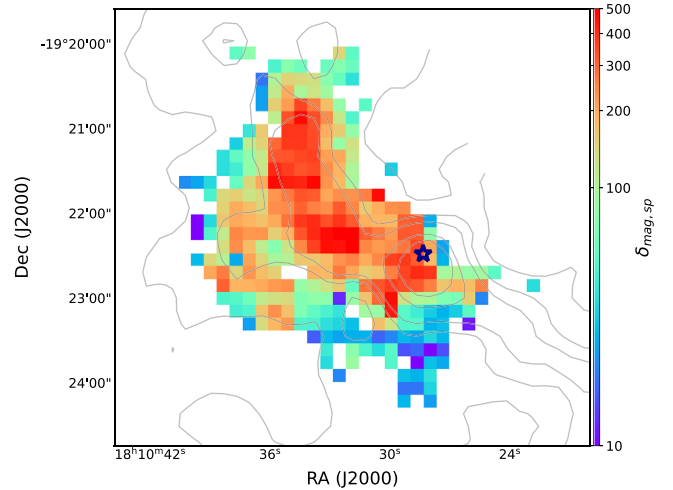


**Figure 19.** Map of $\delta_{\mathrm{mag,sp}}$ for the center region of G11. The value of $\delta_{\mathrm{mag,\ sp}}$ increases from the outer to the inner region and is larger than $\sim 10$. The star marker shows the location of P1.

Figure 4). From Figure 4, one can see that our observations mainly trace the dense region with $N(\mathrm{H}_2) > 10^{22}\,\mathrm{cm}^{-2}$. Therefore, our finding of the perpendicular orientation between $B$-fields and the filament is in agreement with previous studies (Planck Collaboration et al. 2016; Soler & Hennebelle 2017; Soler et al. 2017).

We applied the DCF method to calculate the map of the $B$-field strengths of the center region. The $B$-field strengths vary from 100 to 600 $\mu$G and are strongest close to the filament's spine at high densities. The $B$-field strengths decrease when going from the filament's spine to the outer regions. A previous study by Pillai et al. (2015) using JCMT/SCUPOL measured the lower limit of the $B$-field strength toward the densest region of the center region (see Figure 2) to be $\sim 200\,\mu$G. This value is in the range of our measured $B$-field strengths and in an excellent agreement with our average value $B_{\mathrm{POS}} = 242 \pm 50\,\mu$G estimated from the structure function method.

The $B$-field strengths found for G11 are also comparable to the measurements in other massive filaments, for example, $\sim 50\,\mu$G for G35.39 $-$ 0.33 (Liu et al. 2018), $\sim 100\text{–}800\,\mu$G for NGC 6334 (Arzoumanian et al. 2021), $\sim 60\text{–}470\,\mu$G for

G34.43 + 0.24 (Soam et al. 2019), ∼20–100 $\mu$G for G47.06 + 0.26 (Stephens et al. 2022), and ∼600–1000 $\mu$G for DR21 (Ching et al. 2022).

We quantified the relative role of $B$-fields compared to gravity and turbulence by calculating the mass-to-flux ratio, $\lambda$, and Alfvénic Mach number, $\mathcal{M}_A$. We found that the central region is subcritical, implying that gravity is not strong enough to cause gravitational collapse. Moreover, we found $\mathcal{M}_A < 1$ over most parts of the filament, which implies that $B$-fields dominate over turbulence. This finding is consistent with the idea that the filament is still in its early stages and the influence of $B$-fields on its evolution is important.

## 5.2. Polarization Hole and RAT Alignment

Observations of dust polarization toward different environments usually report the decrease of polarization fraction with increasing total intensity, which is usually referred to as a polarization hole (see, e.g., Pattle & Fissel 2019 for a review). A detailed discussion on the origin of the polarization hole using RAT grain alignment is presented in Hoang et al. (2021).

G11, without bright embedded sources, is an ideal target to provide evidence for the RAT alignment mechanism because the main radiation source for grain heating and alignment is from interstellar radiation fields (Hoang et al. 2021). We found the slope of $P \propto I^{-\alpha}$ with $\alpha \sim 0.8$–$0.9$ for G11, which is much steeper than observed in the massive filament DR21 by JCMT/POL2 ($\alpha \sim 0.3$; Ching et al. 2022) and observed in Serpens South by SOFIA/HAWC+ ($\alpha \sim 0.5$; Pillai et al. 2020). The steep slope in G11 reveals that grain alignment is only efficient in the outer region and becomes significantly lost in the inner region.

In Section 4.5, we prove that the depolarization by $B$-field tangling in this dense filament appears to be a minor effect and must be due to grain alignment. To understand the role of grain alignment in causing the polarization hole effect, we calculated the minimum size for grain alignment by RATs, $a_{\text{align}}$, as a function of the local gas density and radiation field (dust temperature) using the RAT theory (Hoang et al. 2021). We found a tight correlation between the alignment size and the total intensity (Figure 17). Moreover, we found a tight anticorrelation of both polarization fraction, $P$, and the observed alignment efficiency, $P \times \mathcal{S}$, with $a_{\text{align}}$ (Figure 18), implying that the reduced range of alignment size toward the filament's spine is the potential cause of the polarization hole, as expected in the RAT theory (Hoang et al. 2021). Indeed, for dust grains having sizes above $a_{\text{align}}$, their Larmor precession must be faster than the gas damping timescale in order to be stably aligned with $B$-fields (Tram & Hoang 2022). We checked this condition for G11 by calculating the maximum grain alignment sizes for dust grains in the densest regions of G11's spine using Equation (25) of Tram & Hoang (2022). We found that even paramagnetic grains of sizes up to ∼100 $\mu$m can still be efficiently aligned with $B$-fields. Therefore, the reason for the depolarization is not Larmor precession but the reduced RAT alignment efficiency toward the denser region, in contrast to the case of protostellar cores (Giang et al. 2023; Hoang et al. 2022).

## 5.3. On the Role of Magnetic Relaxation on RAT Alignment

Our observational data reveal that the polarization fraction is very high in the outer region of the filament, spanning between 20% and 30% (see Figures 12 and 13). This polarization level is much higher than the average level of the ISM of $P \sim 15\%$ observed by Planck Collaboration et al. (2020), but it is comparable to the observations toward the massive filament DR21 (Ching et al. 2022) and G34.43 (Soam et al. 2019). Previous modeling of Planck data concluded that a high alignment degree of grains is required to reproduce the observational data (Guillet et al. 2018; Hensley & Draine 2023). Therefore, we expect that the higher polarization level observed in the outer regions of massive filaments can be achieved only if grains can be perfectly aligned.

The perfect alignment of grains cannot be achieved by RATs only owing to the dependence of the alignment efficiency on parameters such as the angle between the radiation direction and the $B$-field, the grain shape, and composition (Hoang & Lazarian 2016; Herranen et al. 2021). However, the effect of enhanced magnetic relaxation by grains with iron inclusions is predicted to increase the RAT alignment efficiency (Hoang & Lazarian 2016; Hoang et al. 2022). Using the map of $B$-field strengths obtained by the DCF method, for the first time we observationally estimate the importance of magnetic relaxation and MRAT alignment mechanism in a filament. Due to strong $B$-fields in G11, we found that a small level of iron inclusions (i.e., $N_{\text{cl}} = 100$ and $\phi_{\text{sp}} = 0.01$) can produce the magnetic relaxation faster than the gas randomization with the magnetic relaxation parameter $\delta_{\text{mag,sp}} > 10$ (see Figure 19). In dense regions like the inner filaments close to their spines, one expects the incorporation of iron inclusions into dust grains due to grain collisions and thus larger $\delta_{\text{mag,sp}}$. The significantly enhanced magnetic relaxation combined with RATs can induce perfect alignment for grains with iron inclusions, which could reproduce the high polarization fraction observed toward G11. The importance of MRAT in the Galactic center is also reported by Akshaya & Hoang (2023).

## 5.4. Implications for Grain Growth

Observational studies suggest that the upper limit of the grain size distribution in the ISM is ∼0.25 $\mu$m (Mathis et al. 1977; so-called MRN distribution). However, grain growth is expected to occur in dense molecular clouds. Dust polarization is a useful tracer for grain growth. Previous observations of starlight polarization combined with numerical modeling using the RAT theory in Vaillancourt et al. (2020) reveal grain growth in dense clouds.

In this paper, based on the map of alignment size (Figure 16) and the polarization fraction (Figure 11), we constrain the lower limit for the maximum grain size, $a_{\text{max}}$, of the grain size distribution that is required to reproduce the polarization fraction slope. The outer region has a high polarization fraction (Figure 11); therefore, $a_{\text{max}}$ has to be much larger than $a_{\text{align}} \sim 0.05$–$0.15$ $\mu$m (typical values of $a_{\text{align}}$ in the outer region; see Figure 16). This can be satisfied with the ISM value of $a_{\text{max}} \sim 0.25$ $\mu$m from the MRN distribution. In particular, the estimated slope of $\alpha \sim 0.8$–$0.9 < 1$ (Figure 13) implies that grain alignment is not completely lost ($\alpha = 1$), even in the filament's spine, where the densities are highest. Therefore, there still exist grains that can emit polarized radiation. This is only satisfied when grain growth could occur within the filament, which increases the maximum grain size beyond the $a_{\text{align}}$ values of the filament's spine of 0.30 $\mu$m, namely $a_{\text{max}} > a_{\text{align}} \sim 0.30$ $\mu$m (Figure 16). Thus, we found that grain growth already occurs in the G11 filament with moderate

densities, $n(H_2)$, of the order of $\sim 10^4 \, cm^{-3}$ (Figure 7, left panel).

## 6. Conclusions

In this paper, we report a comprehensive analysis of the polarization data toward G11 taken by the polarimeter SOFIA/HAWC+ at 214 $\mu$m wavelength. We study the $B$-fields' properties and grain alignment's physics in this region. Our main results are summarized as follows:

1. We constructed the map of $B$-fields by rotating the dust polarization angles by $90°$. The $B$-fields are mainly perpendicular to the filament's spine. There is a slow turning of the relative angles between the $B$-fields and the filament's spine from small angles in the lower-density regions to perpendicular in the high-density regions (Figure 4).
2. We derived the map of $B$-field strengths for the center region of the filament using the DCF method. The $B$-field strengths vary from 100 to 600 $\mu$G, with the highest strengths close to the filament's spine of high density and lower strengths in the outer regions of the filament of lower density.
3. We calculated the mass-to-flux ratio and Alfvénic Mach number maps in the center region. These maps show that G11 has strong $B$-fields, which are dominant over turbulence. The central region of the filament is mostly subcritical.
4. We performed different analyses using the dust polarization fraction for the entire Snake filament to constrain grain alignment physics and dust properties. Using the RAT alignment theory, we found that the increase of minimum sizes of dust grains toward the filament center by RAT successfully explains the decrease of the polarization fraction with increasing gas column densities and total intensities. From the alignment efficiency studies taking into account the contribution of the polarization angle dispersion function, the $B$-field tangling seems to be minuscule and cannot explain the depolarization effect in the filament's spine.
5. We constrained the grain growth using the slopes of the polarization fraction versus intensities and RAT alignment theory. In the outer regions, the maximum grain sizes, $a_{max}$, are larger than $a_{align} \sim 0.1 \, \mu$m. In the filament's spine, $a_{max}$ must be larger than the alignment sizes $a_{align} \sim 0.30 \, \mu$m to reproduce the slope of $\alpha \sim 0.8–0.9$.
6. Using the $B$-field strengths measured by the DCF method, we evaluated the importance of magnetic relaxation on RAT alignment. We found that grains can be perfectly aligned by the joint effect of enhanced magnetic relaxation and RATs, which can successfully explain the high polarization fraction in the outer region of G11 with $P \gtrsim 20\%$.

## ORCID iDs

Nguyen Bich Ngoc https://orcid.org/0000-0002-5913-5554
Pham Ngoc Diep https://orcid.org/0000-0002-2808-0888
Thiem Hoang https://orcid.org/0000-0003-2017-0982
Le Ngoc Tram https://orcid.org/0000-0002-6488-8227
Nguyen Chau Giang https://orcid.org/0000-0002-3681-671X
Ngân Lê https://orcid.org/0000-0003-1990-1717
Thuong D. Hoang https://orcid.org/0000-0002-3437-5228
Nguyen Thi Phuong https://orcid.org/0000-0002-4372-5509
Nguyen Minh Khang https://orcid.org/0000-0001-9657-8728
Dieu D. Nguyen https://orcid.org/0000-0002-5678-1008
Bao Truong https://orcid.org/0000-0001-9654-8051

## References

Akshaya, M. S., & Hoang, T. 2023, MNRAS, 522, 4196
Alina, D., Montier, L., Ristorcelli, I., et al. 2016, A&A, 595, A57
Andersson, B., Lazarian, A., & Vaillancourt, J. E. 2015, ARA&A, 53, 501
André, P., Di Francesco, J., Ward-Thompson, D., et al. 2014, in Protostars and Planets VI, ed. H. Beuther et al. (Tucson, AZ: Univ. Arizona Press), 27
Añez-López, N., Busquet, G., Koch, P., et al. 1919, A&A, 644, A52
Arzoumanian, D., Furuya, R., Hasegawa, T., et al. 2021, A&A, 647, A78
Bethell, T. J., Chepurnov, A., Lazarian, A., & Kim, J. 2007, ApJ, 663, 1055
Buckle, J. a., Hills, R., Smith, H., et al. 2009, MNRAS, 399, 1026

Chandrasekhar, S., & Fermi, E. 1953, ApJ, 118, 116
Chapin, E., Gibb, A. G., Jenness, T., et al. 2013, Starlink User Note 258
Ching, T.-C., Qiu, K., Li, D., et al. 2022, ApJ, 941, 122
Crutcher, R. M. 2004, Ap&SS, 292, 225
Crutcher, R. M. 2012, ARA&A, 50, 29
Currie, M., Berry, D., Jenness, T., et al. 2014, in ASP Conf. Ser. 485, Astronomical Data Analysis Software and Systems XXIII, ed. N. Manset & P. Forshay (San Francisco, CA: ASP), 391
Davis, L. 1951, PhRv, 81, 890
Davis, L., Jr, & Greenstein, J. L. 1951, ApJ, 114, 206
Draine, B. T. 2010, Physics of the Interstellar and Intergalactic Medium (Princeton, NJ: Princeton Univ. Press)
Draine, B. T., & Weingartner, J. C. 1997, ApJ, 480, 633
Falceta-Gonćalves, D., Lazarian, A., & Kowal, G. 2008, ApJ, 679, 537
Fissel, L. M., Ade, P. A. R., Angilè, F. E., et al. 2019, ApJ, 878, 110
Giang, N. C., Hoang, T., Kim, J.-G., & Tram, L. N. 2023, MNRAS, 520, 3788
Guerra, J. A., Chuss, D. T., Dowell, C. D., et al. 2021, ApJ, 908, 98
Guillet, V., Fanciullo, L., Verstraete, L., et al. 2018, A&A, 610, A16
Harper, D. A., Runyan, M. C., Dowell, C. D., et al. 2018, JAI, 7, 1840008
Hennebelle, P., & Inutsuka, S.-i. 2019, FrASS, 6, 5
Henney, W. J., Arthur, S. J., De Colle, F., & Mellema, G. 2009, MNRAS, 398, 157
Henning, T., Linz, H., Krause, O., et al. 2010, A&A, 518, L95
Hensley, B. S., & Draine, B. T. 2023, ApJ, 948, 55
Herranen, J., Lazarian, A., & Hoang, T. 2021, ApJ, 913, 63
Hildebrand, R. H., Kirby, L., Dotson, J. L., Houde, M., & Vaillancourt, J. E. 2009, ApJ, 696, 567
Hoang, T., & Lazarian, A. 2008, MNRAS, 388, 117
Hoang, T., & Lazarian, A. 2014, MNRAS, 438, 680
Hoang, T., & Lazarian, A. 2016, ApJ, 831, 159
Hoang, T., Tram, L. N., Lee, H., Diep, P. N., & Ngoc, N. B. 2021, ApJ, 908, 218
Hoang, T., Tram, L. N., Minh Phan, V. H., et al. 2022, AJ, 164, 248
Hu, Y., Yuen, K. H., Lazarian, A., et al. 2019, ApJ, 884, 137
Hwang, J., Kim, J., Pattle, K., et al. 2021, ApJ, 913, 85
Hwang, J., Kim, J., Pattle, K., et al. 2022, ApJ, 941, 51
Jackson, J. M., Finn, S. C., Chambers, E. T., Rathborne, J. M., & Simon, R. 2010, ApJL, 719, L185
Johnstone, D., Fiege, J. D., Redman, R., Feldman, P., & Carey, S. J. 2003, ApJL, 588, L37
Jones, T. J. 1989, ApJ, 346, 728
Jones, T. J., Klebe, D., & Dickey, J. M. 1992, ApJ, 389, 602
Kainulainen, J., Ragan, S., Henning, T., & Stutz, A. 2013, A&A, 557, A120
Koch, E. W., & Rosolowsky, E. W. 2015, MNRAS, 452, 3435
Lazarian, A. 2007, JQSRT, 106, 225
Lazarian, A., & Hoang, T. 2007, MNRAS, 378, 910
Lee, H., Hoang, T., Le, N., & Cho, J. 2020, ApJ, 896, 44
Liu, T., Li, P. S., Juvela, M., et al. 2018, ApJ, 859, 151
Mathis, J. S., Rumpl, W., & Nordsieck, K. H. 1977, ApJ, 217, 425
Matthews, B. C., McPhee, C. A., Fissel, L. M., & Curran, R. L. 2009, ApJS, 182, 143
McKee, C. F., & Tan, J. C. 2003, ApJ, 585, 850
Minamidani, T., Tanaka, T., Mizuno, Y., et al. 2011, AJ, 141, 73
Ngoc, N. B., Diep, P. N., Parsons, H., et al. 2021, ApJ, 908, 10
Ostriker, E. C., Stone, J. M., & Gammie, C. F. 2001, ApJ, 546, 980
Pattle, K., & Fissel, L. 2019, FrASS, 6, 15
Pattle, K., Lai, S.-P., Di Francesco, J., et al. 2021, ApJ, 907, 88
Pattle, K., Ward-Thompson, D., Berry, D., et al. 2017, ApJ, 846, 122
Pillai, T., Kauffmann, J., Tan, J. C., et al. 2015, ApJ, 799, 74
Pillai, T., Wyrowski, F., Menten, K. M., & Krügel, E. 2006, A&A, 447, 929
Pillai, T. G. S., Clemens, D. P., Reissl, S., et al. 2020, NatAs, 4, 1195
Planck Collaboration, Ade, P. A. R., Aghanim, N., et al. 2016, A&A, 586, A138
Planck Collaboration, Aghanim, N., Akrami, Y., et al. 2020, A&A, 641, A12
Rathborne, J. M., Jackson, J., & Simon, R. 2006, ApJ, 641, 3891
Robitaille, T. 2019, APLpy v2.0: The Astronomical Plotting Library in Python, Zenodo, doi:10.5281/zenodo.2567476
Robitaille, T., & Bressert, E. 2012, APLpy: Astronomical Plotting Library in Python, Astrophysics Source Code Library, ascl:1208.017
Robitaille, T. P., Tollerud, E. J., Greenfield, P., et al. 2013, A&A, 558, A33
Serkowski, K. 1974, MExP, 12, 361
Soam, A., Liu, T., Andersson, B., et al. 2019, ApJ, 883, 95
Soler, J. D. 2019, A&A, 629, A96
Soler, J. D., Ade, P. A. R., Angilè, F. E., et al. 2017, A&A, 603, A64
Soler, J. D., & Hennebelle, P. 2017, A&A, 607, A2
Stephens, I. W., Myers, P. C., Zucker, C., et al. 2022, ApJL, 926, L6
Tang, Y.-W., Koch, P. M., Peretto, N., et al. 2019, ApJ, 878, 10
Temi, P., Hoffman, D., Ennico, K., & Le, J. 2018, JAI, 7, 1840011
Thuong, D., Ngoc, N. B., Diep, P. N., et al. 2022, ApJ, 929, 27
Tram, L. N., Bonne, L., Hu, Y., et al. 2023, ApJ, 946, 8
Tram, L. N., & Hoang, T. 2022, FrASS, 9, 923927
Tram, L. N., Hoang, T., Lee, H., et al. 2021, ApJ, 906, 115
Vaillancourt, J. E., Andersson, B.-G., Clemens, D. P., et al. 2020, ApJ, 905, 157
Wang, K., Zhang, Q., Testi, L., et al. 2014, MNRAS, 439, 3275
Ward-Thompson, D., Kirk, J., Crutcher, R., et al. 2000, ApJL, 537, L135
Ward-Thompson, D., Pattle, K., Bastien, P., et al. 2017, ApJ, 842, 66
Whittet, D., Hough, J., Lazarian, A., & Hoang, T. 2008, ApJ, 674, 304
Zucker, C., Battersby, C., & Goodman, A. 2018, ApJ, 864, 153
Zucker, C., & Chen, H. H.-H. 2018, ApJ, 864, 152